Precise Modulation of Triple-Phase Boundaries towards a Highly Functional Exsolved Catalyst for Dry Reforming of Methane under a Dilution-Free System

Jinkyung Oh[+], Sangwook Joo[+], Chaesung Lim, Hyung Jun Kim, Francesco Ciucci,
Jian-Qiang Wang, Jeong Woo Han,* and Guntae Kim*

Abstract: Dry reforming of methane (DRM) has been emerging as a viable solution to achieving carbon neutrality enhanced by the Paris Agreement as it converts the greenhouse gases of CO_2 and CH_4 into industrially useful syngas. However, there have been limited studies on the DRM catalyst under mild operating conditions with a high dilution gas ratio due to their deactivation from carbon coking and metal sintering. Herein, we apply the triple-phase boundary (TPB) concept to DRM catalyst via exsolution phenomenon that can secure elongated TPB by controlling the Fe-doping ratio in perovskite oxide. Remarkably, the exsolved catalyst with prolongated TPB shows exceptional CO_2 and CH_4 conversion rates of 95.9 % and 91.6 %, respectively, stable for 1000 hours under a dilution-free system. DFT calculations confirm that the Lewis acid of support and Lewis base of metal at the TPB promote the adsorption of reactants, resulting in lowering the overall CO_2 dissociation and CH_4 dehydrogenation energy.

Introduction

As the Paris Agreement obliges almost all countries to mitigate greenhouse gas emissions from 2021, diverse reduction and utilization measures have extensively emerged over the past few years.[1–4] Dry reforming of methane (DRM) can be a revolutionary solution in terms of utilizing the top two greenhouse gases of CO_2 and CH_4 at the same time and producing syngas (a mixture of H_2 and CO) with a suitable H_2/CO ratio for Fischer–Tropsch (FT) synthesis.[5–7] Moreover, DRM enables an industry-wide loop by producing syngas feedstock for synthesizing a variety of chemicals.[8,9]

However, the limitations of the catalyst from metal sintering and carbon coking under the operating condition have confined its utilization to the industrial level.[5,10,11] Some catalysts have been reported to have high conversion rates, but in most cases dilution gases (e.g., nitrogen or inert gas) still need to be added to the reactants for higher catalytic activity and stability.[5,6] The process requiring dilution gases is very inefficient when considering extra addition and separation processes, consequently increasing overall maintenance cost. The focus of DRM research, therefore, is shifting towards searching for highly active and durable catalysts without any dilution gases.[12–14]

Meanwhile, triple-phase boundary (TPB) as the interfacial active site where a gaseous reactant, electronic conductor, and ionic conductor intersect has been studied extensively in the field of electrochemistry (for example, $O_2(g)$, electron, and O^{2-} for oxygen reduction reaction in conducting oxide energy system, such as solid oxide fuel cells),[15–17] but it has not been fully studied in other fields such as thermochemistry. In the DRM thermochemical reaction, for example, both CO_2 and CH_4 undergo the adsorption followed by dissociation steps, and it is known that each step occurs mainly on support and metal, respectively.[18,19] That is, the interface between support and metal in DRM can be interpreted as TPB (reactant gases, dissociation promoting metal, and adsorption promoting support). Thus, TPB could be envisaged as a measurable parameter of the materials for devising active and stable catalysts towards DRM, given that the interfacial site

[*] J. Oh,[+] S. Joo,[+] Prof. G. Kim
School of Energy and Chemical Engineering
Ulsan National Institute of Science and Technology (UNIST)
Ulsan, 44919 (Republic of Korea)
E-mail: gtkim@unist.ac.kr

C. Lim, H. J. Kim, Prof. J. W. Han
Department of Chemical Engineering
Pohang University of Science and Technology (POSTECH)
Pohang, 37673 (Republic of Korea)
E-mail: jwhan@postech.ac.kr

F. Ciucci
Department of Chemical and Biological Engineering
The Hong Kong University of Science and Technology
Clear Water Bay, Hong Kong (China)

J.-Q. Wang
Key Laboratory of Interfacial Physics and Technology
Shanghai Institute of Applied Physics
Chinese Academy of Sciences
Shanghai 201800 (China)

[+] These authors contributed equally to this work.

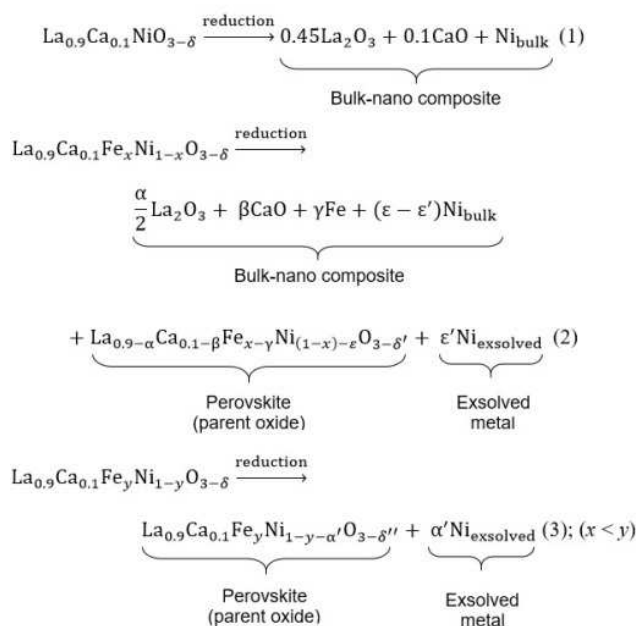between support oxide and metal particle plays an important role besides the metallic site in DRM.[20,21]

In this context, exsolution may provide a reasonable tool to prepare supported metal nanocatalysts to obtain extended TPB. This exsolution method allows the formation of nanocatalysts by spontaneous phase separation of metal particles on nanoscale near the surface,[22] which provides a very unique interface between the two phases of the embedded nanoparticles and the parent oxide.[23] This unique interface distinguishes the exsolved nanocatalysts from classical supported metal catalysts forming relatively shallow interfaces with the oxide support.[23] Therefore, understanding and manipulating the interfacial site at the perimeter of the exsolved nanoparticles is of great significance, taking into account that it acts as TPBs, thereby substantially influencing the activity and stability of the catalyst.[24]

Herein, we report a highly active and stable catalyst for DRM under a dilution-free system by achieving the utmost interfacial properties driven by exsolution. The Fe-doped lanthanum calcium nickelate is chosen for this case study because it displays the delicate interfacial nature between the bulk-nano composite catalyst and the exsolved nano-catalyst under reducing conditions. For example, in the case of $LaNiO_{3-\delta}$, it is separated by La_2O_3 support oxides and metallic Ni as pO_2 decreases. Until now, $LaNiO_{3-\delta}$ catalysts have been employed as Ni metal deposited on La_2O_3 support,[21,25–30] and thus it still retains the limitations of stability due to the particle agglomeration as a conventional supported metal catalyst. Conversely, we incorporate Fe into Ca-doped $LaNiO_{3\delta}$ to induce a phase transition from bulk-nano composite catalyst to exsolved nanocatalyst. In this way, exsolved Ni nanoparticles on perovskite oxide support can manifest the characteristic of exsolution, securing the utmost interfacial properties of exsolution. The most prolonged interfacial perimeter around the as-exsolved particles shows more than 91.6 % of CH_4 conversion and 95.9 % of CO_2 conversions for 1000 hours at 850 °C with no dilution gas as the best-in-class DRM performance. Our theoretical analysis also confirms that the robust catalytic activity of the interfacial site of the exsolved nanoparticles originates from the coexistence of Lewis base (exsolved nanoparticle) and Lewis acid (support). The coexistence of Lewis base and Lewis acid mediates the strong chemisorption of CO_2 in the form of CO_3^{2-} through the easy electron transfer from exsolved nanoparticle to the support. It also facilitates CH_4 dehydrogenation by providing both the dehydrogenation site (Lewis acid) and adsorption site (Lewis base) of the methyl radical. As a result, the more elongated TPB is secured, the better catalytic activity in the DRM field can be obtained.

Results and Discussion

In this study, we design the exsolved catalysts for DRM with different degrees of the interface between the exsolved metal and the perovskite oxide support by varying the Fe ratio, which in turn provides controllable TPB in the thermochemistry field. As a case study to induce a phase transition from the bulk-nano composite to exsolution securing TPBs, we choose $La_{0.9}Ca_{0.1}NiO_{3-\delta}$ as a starting catalyst that forms bulk-nano composite under reducing conditions. By doping Fe to the catalyst, we assume that the phases can be conceptually classified into three zones: a bulk-nano composite zone in which Ni in the lattice is separated to become bulk Ni particles [Eq. (1)], a mixed phase zone where lattice Ni is partially separated and begins to coexist with exsolved Ni particles at the Fe-doping ratio of x [Eq. (2)], and an exsolution zone where a single phase of perovskite exists with Ni particles anchored on the surface of the perovskite oxide at a higher Fe-doping ratio of y [Eq. (3)].

$$La_{0.9}Ca_{0.1}NiO_{3-\delta} \xrightarrow{reduction} \underbrace{0.45La_2O_3 + 0.1CaO + Ni_{bulk}}_{\text{Bulk-nano composite}} \quad (1)$$

$$La_{0.9}Ca_{0.1}Fe_xNi_{1-x}O_{3-\delta} \xrightarrow{reduction}$$

$$\underbrace{\frac{\alpha}{2}La_2O_3 + \beta CaO + \gamma Fe + (\varepsilon - \varepsilon')Ni_{bulk}}_{\text{Bulk-nano composite}}$$

$$+ \underbrace{La_{0.9-\alpha}Ca_{0.1-\beta}Fe_{x-\gamma}Ni_{(1-x)-\varepsilon}O_{3-\delta'}}_{\substack{\text{Perovskite} \\ \text{(parent oxide)}}} + \underbrace{\varepsilon'Ni_{exsolved}}_{\substack{\text{Exsolved} \\ \text{metal}}} \quad (2)$$

$$La_{0.9}Ca_{0.1}Fe_yNi_{1-y}O_{3-\delta} \xrightarrow{reduction}$$

$$\underbrace{La_{0.9}Ca_{0.1}Fe_yNi_{1-y-\alpha'}O_{3-\delta''}}_{\substack{\text{Perovskite} \\ \text{(parent oxide)}}} + \underbrace{\alpha'Ni_{exsolved}}_{\substack{\text{Exsolved} \\ \text{metal}}} \quad (3); (x < y)$$

According to Equation (2), the introduction of Fe contributes to suppressing perovskite phase decomposition,[31,32] resulting in a phase transition to the mixed phase zone. Moreover, when the Fe ratio exceeds a specific value of y, the phase is further shifted towards the exsolution zone where all the metal particles are embedded on the surface of the parent perovskite oxide [Eq. (3)].

To induce different degrees of exsolution, we synthesized different Fe ratios of perovskite structure samples, $La_{0.9}Ca_{0.1}Fe_xNi_{1-x}O_{3-\delta}$ ($x = 0, 0.4, 0.5, 0.6$, and 0.7) sintered at 950 °C in air (Figure S1). The main peak is shifted to a lower 2θ angle with an increasing amount of Fe due to a larger ionic radius of Fe ions compared to Ni ions,[33] resulting in an increased unit cell volume of the perovskite structure (Table S1). At a Ni-rich composition of air-sintered $La_{0.9}Ca_{0.1}Fe_{0.3}Ni_{0.7}O_{3-\delta}$ ($x = 0.3$), NiO peak is detected due to the limited solubility of B-site cations in the lattice (Figure S2). As a result, an exsolution system with a Fe content of less than 0.4 is investigated to induce the three zones mentioned above. The samples are abbreviated to represent each composition and are summarized in Table 1.

Table 1: Chemical compositions and abbreviations of the samples.

Compound	Abbreviations
Reduced $La_{0.9}Ca_{0.1}NiO_{3-\delta}$	LCN
Reduced $La_{0.9}Ca_{0.1}Fe_{0.4}Ni_{0.6}O_{3-\delta}$	LCFN46
Reduced $La_{0.9}Ca_{0.1}Fe_{0.5}Ni_{0.5}O_{3-\delta}$	LCFN55
Reduced $La_{0.9}Ca_{0.1}Fe_{0.6}Ni_{0.4}O_{3-\delta}$	LCFN64
Reduced $La_{0.9}Ca_{0.1}Fe_{0.7}Ni_{0.3}O_{3-\delta}$	LCFN73
Reduced $La_{0.9}Ca_{0.1}FeO_{3-\delta}$	LCF

To verify the TPB length varied with the degree of exsolution, the correlation between the interfacial perimeter of exsolved nanoparticles and Fe-doping ratio is investigated through scanning electron microscopy (SEM) and transmission electron microscopy (TEM). The SEM images in Figure 1a reveal that various Fe-doping (Fe = 0.4–0.7) induces different sizes and populations of exsolved particles. At the Fe ratio of LCFN46, exsolved particles are formed but still coexist with decomposed phases (Figure S3). With the increased Fe ratio to LCFN55, the size of the exsolved
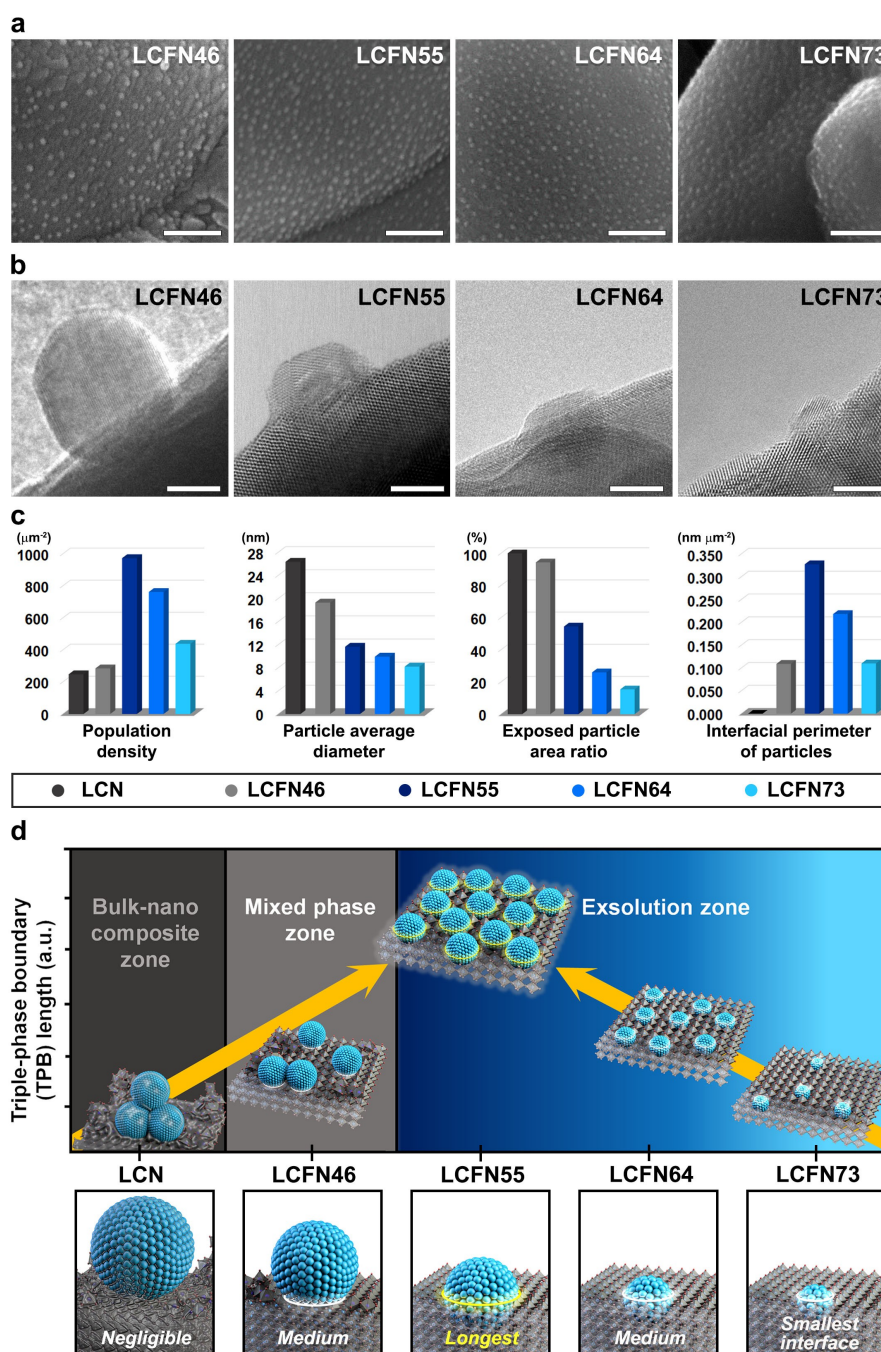
Figure 1. Particle characteristics varied with Fe-doping. a) SEM images and b) TEM images of Fe-doped samples; scale bars are 200 nm and 5 nm, respectively. c) Sample characterization graphs based on SEM and TEM images.
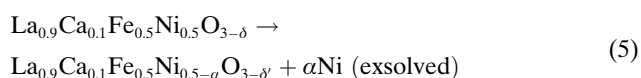
particles decreases, and the number of the exsolved particles increase significantly without any decomposed phases. However, a higher Fe dopant ratio (Fe > 0.5) appears to deteriorate the formation of nanoparticles given the decreased population and size of the exsolved particles in LCFN64 and LCFN73. Interestingly, TEM analysis shows that increasing the Fe dopant makes the particles more immersed in the support (Figure 1b). These results suggest that the amount of Fe dopant can affect the control parameters of nanoparticles, such as population, size, and anchorage, which are closely related to the TPB length.

For a more precise investigation of the TPB on each sample, the nanoparticles in a specific area are quantitatively analyzed with ImageJ software. LCN is additionally analyzed for a comparison with the Fe-doped samples (Figure S4), and its particle interfacial perimeter is assumed to be near zero as the deposited particles are mobile and form shallow interfaces with support.[23] Figure 1c shows the particle characteristics of LCFN46 are not much deviated from those of LCN, yet at LCFN55, the number of the particle increases rapidly up to 980 particles μm^{-2} with largely reduced particle size and anchorage degree (calculated from exposed particle area ratio). This implies that the phase has been shifted to the exsolution zone from LCFN55. On the other hand, the population, size, and anchorage decrease from LCFN64, resulting in the longest particle interfacial perimeter of 0.328 nm μm^{-2} at LCFN55. That is, the most elongated TPB is obtained at LCFN55.

Figure 1d depicts the volcano-like trend of the TPB with respect to the Fe-doping ratio: the length of TPB increases and then decreases with increasing the amount of Fe. The interfacial perimeter (e.g., interfacial perimeter = population × average particle perimeter) reaches a maximum at LCFN55 by phase-shifting from bulk-nano composite zone to exsolution zone. As illustrated below, the depth of a single particle becomes deeper as Fe increases, and thus the interface varying with depth increases. However, when the Fe-doping ratio exceeds that of LCFN55, the length of TPB starts to decrease, implying that it can be controlled and maximized by altering the exsolution degree.

The LCFN55 sample with the longest TPB length was characterized in comparison with the conventional support catalyst of LCN. The air-sintered $La_{0.9}Ca_{0.1}Fe_{0.5}Ni_{0.5}O_{3-\delta}$ and $La_{0.9}Ca_{0.1}NiO_{3-\delta}$ samples are analyzed with in situ X-ray diffraction (in situ XRD) with a 25 °C interval from 700 °C to 850 °C in humidified H_2 conditions. As shown in Figure 2a–d, the diffraction pattern of perovskite is shown for each sample at 30 °C. However, different phase properties appear under reducing conditions as below;

$$La_{0.9}Ca_{0.1}NiO_{3-\delta} \rightarrow$$
$$0.9La_2O_3 + 0.1CaO + Ni \text{ (mobile bulk)} \tag{4}$$

$$La_{0.9}Ca_{0.1}Fe_{0.5}Ni_{0.5}O_{3-\delta} \rightarrow$$
$$La_{0.9}Ca_{0.1}Fe_{0.5}Ni_{0.5-\alpha}O_{3-\delta'} + \alpha Ni \text{ (exsolved)} \tag{5}$$

According to Equation (4) and (5), the secondary phase peak of La_2O_3 can be a key indicator for determining the degree of phase transition and the presence of TPB active

sites. The La_2O_3 peak of air-sintered $La_{0.9}Ca_{0.1}NiO_{3-\delta}$ starts to be detected clearly from 700 °C and increases rapidly so that the perovskite phase almost disappears at 850 °C (see the main peak at $2\theta = 32°$), suggesting that the undoped sample (LCN) tends to undergo phase decomposition more easily and thus hardly retain TPB as shown in Figure 2a and b. In contrast, air-sintered $La_{0.9}Ca_{0.1}Fe_{0.5}Ni_{0.5}O_{3-\delta}$ starts to have a La_2O_3 peak at 775 °C and its peak remains very small up to 850 °C (Figure 2c and d), implying that LCFN55 has a higher resistance against the phase decomposition. In addition, since the exsolution is known to be promoted with increasing temperature, the maximized TPB active site is obtained at 750 °C without any La_2O_3 peaks.

The property to secure TPB is also analyzed through the reduction property analysis of temperature-programmed reduction with H_2 (H_2-TPR). As shown in Figure S5a, $La_{0.9}Ca_{0.1}NiO_{3-\delta}$ follows three reduction pathways, yet four for $La_{0.9}Ca_{0.1}Fe_{0.5}Ni_{0.5}O_{3-\delta}$. Below 600 °C, for $La_{0.9}Ca_{0.1}Fe_{0.5}Ni_{0.5}O_{3-\delta}$ three peaks are associated with the reduction of Ni^{3+} to Ni^{2+} and Fe^{4+} to Fe^{2+} when considering the peaks at $La_{0.9}Ca_{0.1}NiO_{3-\delta}$[34,35] and $La_{0.9}Ca_{0.1}FeO_{3-\delta}$,[36] respectively (Figure S5a and S6). Near 800 °C, the α peaks can be ascribed as the reduction of Ni^{2+} to Ni mainly as it is absent from the reduced samples in Figure S5b where the peak attributed to bulk (near 1000 °C) exists only. Here, it is worth noting that the α peak of LCFN55 is shifted towards a higher temperature, implying that structural stability is enhanced to maintain perovskite oxide with exsolved nanoparticles, which is consistent with in situ XRD data.

X-ray photoelectron spectroscopy (XPS) was conducted to analyze the surface oxidation state of Ni species of LCFN55 compared to LCN (Figure 2e and f). As the La $3d_{3/2}$ and Ni $2p_{3/2}$ spectra overlap at high binding energy, the Ni $3p_{3/2}$ spectra at around 67 eV are analyzed.[37,38] The atomic ratio of Ni metal to total Ni species of LCN is over 90%, implying that most of the Ni species in LCN are segregated from the perovskite lattice to mainly exist as supported catalysts. LCFN55, on the other hand, has a relatively lower Ni metal ratio of 37.5%, indicating that LCFN55 is more likely to maintain mainly the ABO_3 perovskite framework with exsolved metal particles.

The surfaces of the samples are more precisely analyzed through scanning transmission electron microscopy with energy-dispersive X-ray spectroscopy (STEM-EDS) elemental map. Figure 2g, h show the contrasting status of Ni metal on the surface: The Ni metals in the LCN sample are deposited on the surface with a size of around 30 nm, whereas those in the LCFN55 sample are socketed with a uniform distribution on the support with a size of around 15 nm. Most of the Ni from the B-site of LCN is segregated out of the support to form Ni deposited on La_2O_3 (Figure 2g and i), consistent with the XPS data. On the other hand, for the case of LCFN55 only partial Ni has been exsolved from the lattice and anchored on the surface of support, and La, Ca, Fe, Ni, and O elements are detected evenly throughout the parent oxide (Figure 2h and j), implying the maintenance of the perovskite oxide phase. Overall, these results highlight that exsolution phenomena can promote TPB
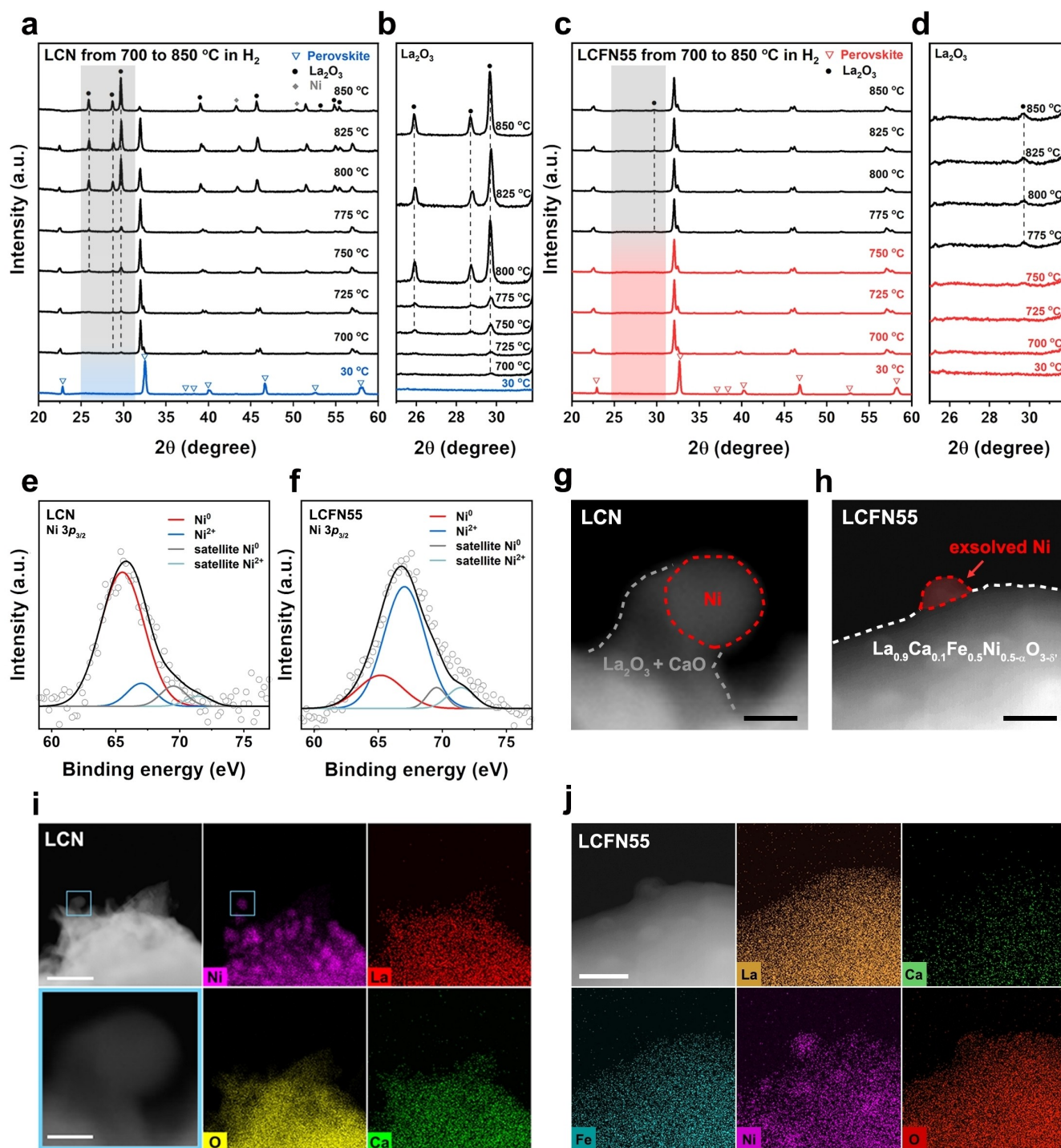
Figure 2. Characterizations of LCN and LCFN55 using in situ XRD, H_2-TPR, and STEM. In situ XRD and its enlarged plots of a), b) LCN and c), d) LCFN55 from 700°C to 850°C under reducing conditions. XPS of e) LCN and f) LCFN55. STEM-HADDF images of g) LCN and h) LCFN55; scale bars are 15 nm. STEM-HADDF images and EDS elemental map of i) LCN and j) LCFN55; scale bars are 250 nm and 25 nm, respectively. The STEM-HADDF image of LCN was magnified in the sky-blue box in (i); scale bar is 25 nm.

active site formation by securing immobile nanoparticles on perovskite support.

To verify the DRM catalytic performance of the LCFN55 compared to the undoped sample of the LCN, the catalytic activities of the samples were tested in the temperature range of 600°C to 750°C under a gas hourly space velocity (GHSV) of $30\,000\,mL\,g^{-1}\,hour^{-1}$ with the gas mixture of CO_2, CH_4, and He of 20, 20, and $60\,mL\,min^{-1}$, respectively. About 60 vol% of dilution gas is introduced to identify the initial active site while minimizing the degradation of the catalyst by carbon coking. Since the dilution gas lowers the concentration of the overall reactant gases, it can

be assumed that the reactants can participate in the reaction without any other factors that lower the activity, allowing to analyze the original active site of the catalyst. The CO_2 and CH_4 conversions are calculated by dividing the concentration of the consumed reactants by that of the injected reactants. As shown in Figure 3a and b, the CO_2 and CH_4 conversion rates of the LCFN55 with the most elongated TPB improve over the entire temperature range compared to the LCN, so it is presumed that TPB plays a key role in the catalytic activity. To identify this presumption, the

catalytic activity of the NiO sample without any TPB sites was evaluated towards DRM. As shown in Figure S7, the catalytic activity of NiO is the lowest over the entire temperature range among the samples, indicating that TPB contributes to high catalytic activity. LCN is decomposed into La_2O_3 and Ni to form coalescence-prone mobile Ni particles that limit the metal active site [Eq. (4)]. On the other hand, embedded Ni particles on the surface of the perovskite oxide of the LCFN55 [Eq. (5)] suppress particle agglomeration and contribute to securing the TPB. Further-
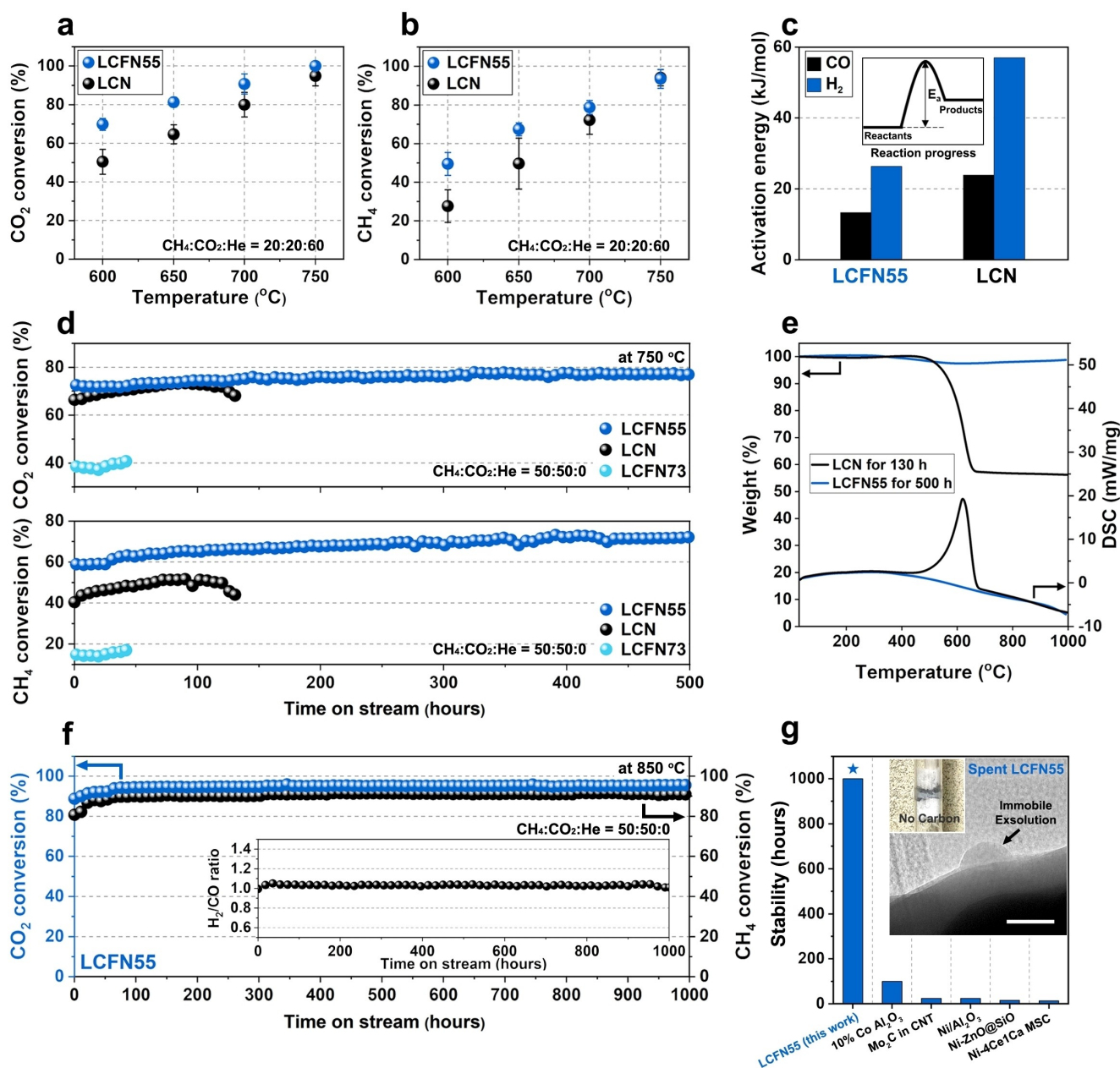
Figure 3. Catalytic activity of LCFN55 compared with LCN. DRM catalytic activity of a) LCN and b) LCFN55. c) Activation energy to produce H_2 and CO for LCN and LCFN55 in the temperature range of 600 °C to 750 °C. d) Continuous DRM operation comparison of LCN and LCFN55 at 750 °C without dilution gas. e) TGA-DSC of LCN and LCFN55 after stability test at 750 °C for 130 hours and 500 hours, respectively. f) Continuous DRM operation of LCFN55 at 850 °C without dilution gas. g) Comparison of long-term stability at 850 °C from the present work to other studies; the inset shows the LCFN55 sample in quartz tube after the continuous DRM reaction at 850 °C for 1000 hours and its TEM image; scale bar is 20 nm.

more, considering that the activation energies of H_2 and CO are lower in LCFN55 than LCN (Figure 3c), it can be deduced that H_2 and CO are produced more favorably at TPB active site than the metal site.

A long-term continuous DRM measurement was performed under a non-diluted gas system with a mixture of the CH_4 and CO_2 ratio of 50:50 at 750 °C to confirm the effect of carbon coking and particle agglomeration with time. In the absence of dilution gases, the degradation of catalytic performance due to the carbon coking and thus particle agglomeration can occur more predominantly. As shown in Figure 3d, the CO_2 and CH_4 conversions of the LCFN55 continue to increase over 500 hours, reaching 77 % and 72 %, respectively, while the conversion values of the LCN decline sharply after 100 hours and those of the LCFN73 are significantly low from the initial stage. Thermogravimetric analysis (TGA) and differential scanning calorimetry (DSC) were carried out to determine the presence of carbon formation in the samples after continuous DRM operations. The curve on the left axis of Figure 3e represents the weight change of the samples after the long-term stability test with increasing temperature in air. The LCN sample experiences a large weight reduction of 43.8 wt % with an exothermic DSC peak,[39] indicating the presence of large carbon coking in the LCN after DRM test. The LCFN55 sample, on the other hand, shows negligible weight loss with no exothermic DSC curve, confirming that the secured TPB with exsolution catalyst can suppress carbon coking and maintain high conversion rates even under the non-diluted DRM system. Besides, an energy dispersive spectroscopy (EDS) line profile for LCFN55 confirms that Ni nanoparticles are strongly anchored on the surface of the perovskite oxide after 500 hours of continuous DRM operation (Figure S8).

We further investigated the continuous DRM operation for the LCFN55 sample without any dilution gases at an elevated temperature of 850 °C. As illustrated in Figure 3f, CH_4 and CO_2 conversions of LCFN55 almost approach the thermodynamic equilibrium of 94.3 % and 97.2 % with 91.6 % and 95.9 %, respectively, with H_2/CO ratio close to unity. Remarkably, the conversions last for more than 1000 hours without deactivation, an unprecedented world record. Some recent studies have been conducted to approach high conversion rates without dilution gases, but they have only been able to operate for a short period of time (<100 hours) and some suffer from severe deactivations[40–44] (Figure 3g). After the long-term stability test, the presence of carbon coking and particle agglomeration is analyzed with TGA-DSC and EDS. As shown in Figure 3g, the glass fiber wool surrounding the sample in the fixed-bed tube is clean and no weight loss in TGA-DSC (Figure S9a) was observed, suggesting that no carbon coking occurs. Also, immobile nanoparticles embedded in the perovskite oxide support in Figure 3g and S9b confirm the higher resistance to metal particle agglomeration and secured TPB over the long operation time to maintain the incredibly high conversion rates. Overall, the LCFN55 with elongated TPB is proven to be highly active and durable without carbon coking and metal particle agglomeration.

To reveal the enhanced catalytic activity of the elongated TPB in DRM reaction, DFT calculations were performed. The major elementary steps of DRM reaction (CO_2 and CH_4 adsorption and dissociation) are compared at the active sites constituting exsolved nanocatalyst; metal and interface (Figure 4a, b and Table 2). As shown in Figure 4a, the CO_2 dissociation is more favorable at the interface than on metal due to the largely reduced CO_2 adsorption energy. In contrast to metal forming weak physisorption ($E_r = 0.01$ eV), the interface forms stronger chemisorption with CO_2 ($E_r = -0.62$ eV) in CO_3^{2-}. To elucidate the origin of the enhanced CO_2 adsorption ability of the interface, the effective Bader charge analysis was performed to quantify electron transfer during adsorption. As illustrated in Figure S10a, electrons are accumulated (red region) at lattice oxygen, while electrons are depleted (blue region) at the adjacent exsolved Ni nanoparticle and CO_2 molecule. Besides exsolved Ni nanoparticle facilitating CO_3^{2-} formation by donating electrons to the oxygens of CO_2, lattice oxygen from oxide support functions as strong Lewis acid by accepting electrons from adsorbed CO_2 (Figure S10b). That is, due to the coexistence of Lewis base of metal and Lewis acid of support, CO_2 adsorption is more favorable at TPB than metal only with Lewis base, resulting in the most active site for CO_2 overall dissociation reaction. Therefore, the longer the TPB length is guaranteed, the higher the CO_2 conversion rate can be obtained.

Figure 4b shows the reaction energies of the CH_4 dehydrogenation including a series of five reaction steps at metal and the interface. The entire CH_4 dehydrogenation reaction ($CH_4 \rightarrow CH_3 \rightarrow CH_2 \rightarrow CH \rightarrow C$) is observed to be more favorable at the interface than at metal. The origin of the enhanced CH_4 dehydrogenation ability of the interface lies in the largely reduced first dehydrogenation step of CH_4 ($E_r = -0.85$ eV, denoted as I2), which is the lowest of all dehydrogenation energies. The first dehydrogenated CH_3 can be regarded as the actual adsorption site for CH_4 dehydrogenation as it forms chemisorption, in contrast to CH_4 forming weak physisorption. That is, the reduced entire CH_4 dehydrogenation energy at the interface stems from improved adsorption ability. For the case of the metal, electrons are transferred from the Ni metal to adsorbed CH_3 (0.27 e) and H (0.26 e), namely metal functions as Lewis base (Figure 4c and d). Meanwhile, at the interface electron is mainly transferred from exsolved nanoparticle to ad-

Table 2: Adsorption and dissociation energies of CO_2 and CH_4 at metal and interface.

Reaction	Reaction energy [eV]	
	Metal	Interface
CO_2 (g)→*CO_2	0.01	−0.62
*CO_2→*O + *CO	−1.05	−0.67
CH_4 (g)→*CH_4	0.06	−0.01
CH_4→CH_3 + *H	−0.14	−0.85
*CH_3 + *H→*CH_2 + *2 H	−0.07	−0.24
*CH_2 + *2 H→*CH + *3 H	−0.42	−0.30
*CH + *3 H→*C + *4 H	0.49	0.26
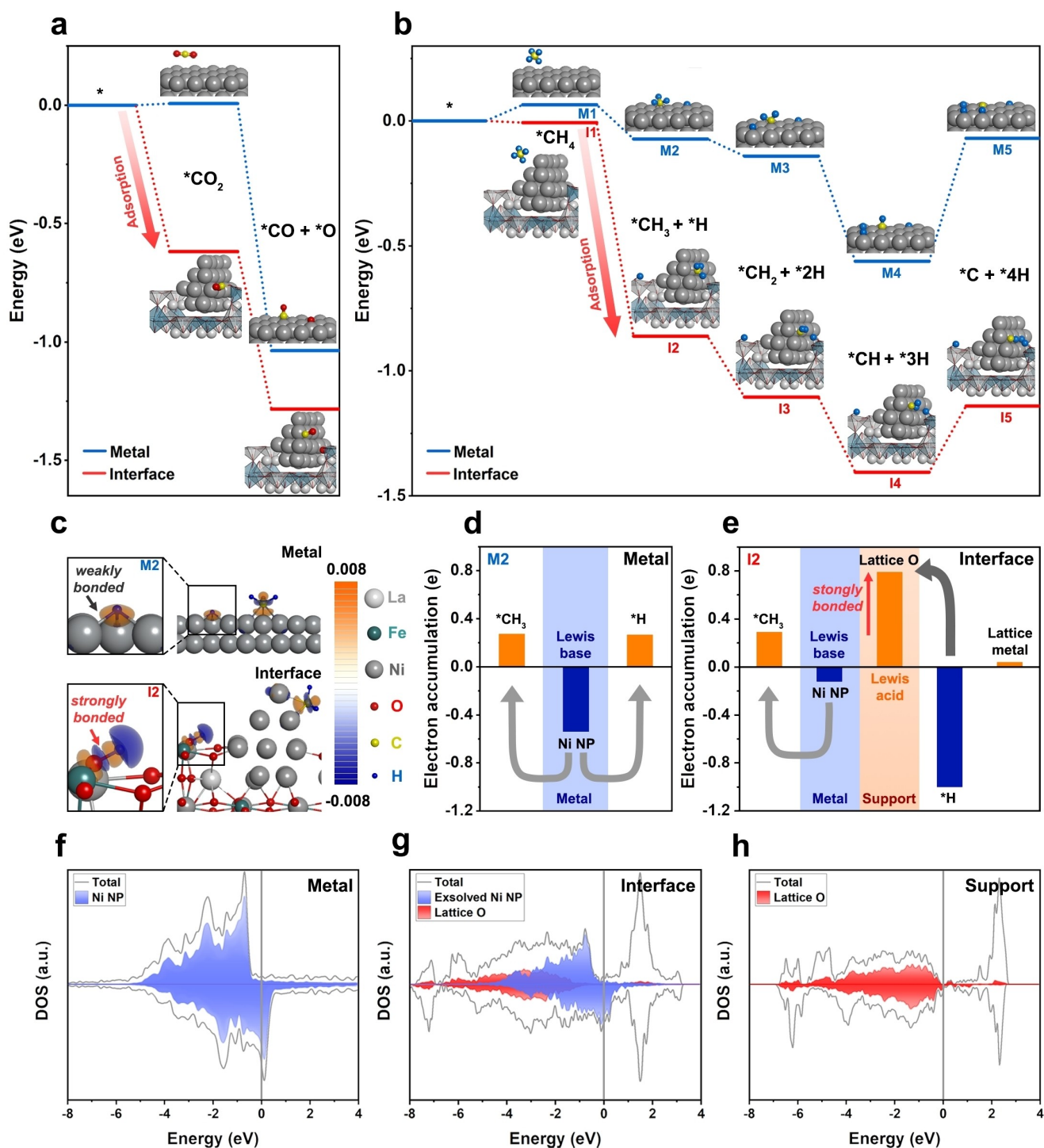
Figure 4. Reaction energy profile of a) CO_2 dissociation and b) CH_4 dehydrogenation at metal and interface. The colour for each atom in the model is white, grey, yellow, blue, and red for La, Ni, C, H, and O atoms, respectively. Grey and blue octahedrons are NiO_6 and FeO_6 octahedrons, respectively. c) Charge density difference upon the H and CH_3 (adsorption site of CH_4) at metal and interface. Orange and navy-blue regions indicate electron accumulation and depletion, respectively. Charge transfer upon the adsorbed H and CH_3 at d) metal and e) interface. Density of states of f) Ni metal, g) interface, and h) perovskite oxide support. The Fermi level is set to zero.

sorbed CH_3 (0.29 e) and from H to lattice oxygen (0.79 e), respectively (Figure 4c and e). Notably, besides exsolved Ni nanoparticle acting as Lewis base, lattice oxygen from support acts as strong Lewis acid, resulting in stronger H adsorption with lattice oxygen. Since more electrons con-

tributing to the adsorption are accumulated at the interface in the first dehydrogenation step of CH_4, the interface is more likely to generate the CH_4 dehydrogenation site of CH_3. Also, more electrons participate in the chemisorption of CH_3 with the exsolved Ni nanoparticle at the interface

than at the metal site. Likewise, the interface is confirmed to function as the most powerful active site of TPB for CH_4 dehydrogenation as it enhances the adsorption ability of CH_4 by promoting CH_3 formation and adsorption at the interface.

Furthermore, the dissociation ability of TPB is investigated by comparing the electron structure of metal and support, constituting TPB. Since the *d*-band center of exsolved Ni nanoparticle (-1.50 eV) is similar to the *d*-band center of Ni metal (-1.20 eV) (Figure 4f and g), it can be deduced that the interface has excellent CO_2 dissociation and CH_4 dehydrogenation ability as metal. Also, as illustrated in Figure 4g and h, the O *p*-band center of the interface (-3.36 eV) is downshifted compared to that of support (-2.27 eV). The downshift of DOS on the interface is caused by the upshift of Fermi level (support: -0.01 eV, interface: 1.15 eV) due to the oxygen defect at the interfacial site,[45] resulting in the reduced CO_2 dissociation energy.

Conclusion

In summary, we have extended the TPB concept from the electrochemical field to the thermochemical field by demonstrating exsolved nanocatalyst for DRM. The TPB is controlled by varying the exsolution degree with the Fe-doping ratio of perovskite oxide. LCFN55 with the most elongated TPB results in the unprecedented CO_2 and CH_4 conversion of 95% and 91%, respectively, stable for 1000 hours under a non-diluted system without any deactivation. The TPB is calculated to be the most active site in DRM reaction as it lowers adsorption energy of CO_2 and CH_4 with Lewis base nature (exsolved metal) and Lewis acid nature (support), inducing more charges to participate during adsorption. Establishing the TPB concept in DRM with the exsolved nanocatalyst opens up a new perspective in designing highly active and durable metal-supported catalysts in the thermochemistry field, which goes beyond the study on exsolution.

Acknowledgments

Conflict of Interest

The authors declare no conflict of interest.

Data Availability Statement

The data that support the findings of this study are available in the Supporting Information of this article.

[1] W. Jang, J. Shim, H. Kim, S. Yoo, H. Roh, *Catal. Today* **2019**, *324*, 15–26.

[2] G. Ji, J. G. Yao, P. T. Clough, J. C. D. da Costa, E. J. Anthony, P. S. Fennell, W. Wang, M. Zhao, *Energy Environ. Sci.* **2018**, *11*, 2647–2672.

[3] S. Joo, K. Kim, O. Kwon, J. Oh, H. J. Kim, L. Zhang, J. Zhou, J. Wang, H. Y. Jeong, J. W. Han, G. Kim, *Angew. Chem. Int. Ed.* **2021**, *60*, 15912–15919; *Angew. Chem.* **2021**, *133*, 16048–16055.

[4] H. Xiong, A. K. Datye, Y. Wang, *Adv. Mater.* **2021**, *33*, 2004319.

[5] Y. Song, E. Ozdemir, S. Ramesh, A. Adishev, S. Subramanian, A. Harale, M. Albuali, B. A. Fadhel, A. Jamal, D. Moon, S. H. Choi, C. T. Yavuz, *Science* **2020**, *367*, 777–781.

[6] S. Das, J. Ashok, Z. Bian, N. Dewangan, M. H. Wai, Y. Du, A. Borgna, K. Hidajat, S. Kawi, *Appl. Catal. B* **2018**, *230*, 220–236.

[7] S. Das, S. Bhattar, L. Liu, Z. Wang, S. Xi, J. J. Spivey, S. Kawi, *ACS Catal.* **2020**, *10*, 12466–12486.

[8] M. Li, B. Hua, J.-L. Luo, *ACS Energy Lett.* **2017**, *2*, 1789–1796.

[9] O. R. Inderwildi, S. J. Jenkins, D. A. King, *Angew. Chem. Int. Ed.* **2008**, *47*, 5253–5255; *Angew. Chem.* **2008**, *120*, 5332–5334.

[10] T. D. Gould, M. M. Montemore, A. M. Lubers, L. D. Ellis, A. W. Weimer, J. L. Falconer, J. W. Medlin, *Appl. Catal. A* **2015**, *492*, 107–116.

[11] J. W. Han, C. Kim, J. S. Park, H. Lee, *ChemSusChem* **2014**, *7*, 451–456.

[12] M. Wang, T. Zhao, X. Dong, M. Li, H. Wang, *Appl. Catal. B* **2018**, *224*, 214–221.

[13] P. Djinović, A. Pintar, *Appl. Catal. B* **2017**, *206*, 675–682.

[14] Q. Chen, J. Zhang, B. Pan, W. Kong, Y. Chen, W. Zhang, Y. Sun, *Chem. Eng. J.* **2017**, *320*, 63–73.

[15] B. Hua, N. Yan, M. Li, Y. Zhang, Y. Sun, J. Li, T. Etsell, P. Sarkar, K. Chuang, J.-L. Luo, *Energy Environ. Sci.* **2016**, *9*, 207–215.

[16] R. O'Hayre, F. B. Prinz, *J. Electrochem. Soc.* **2004**, *151*, A756.

[17] J. Pan, Y. Ye, M. Zhou, X. Sun, Y. Ling, K. Yashiro, Y. Chen, *Materials Reports: Energy* **2021**, *1*, 100025.

[18] R. Besson, M. Rocha Vargas, L. Favergeon, *Surf. Sci.* **2012**, *606*, 490–495.

[19] S. G. Wang, X. Y. Liao, J. Hu, D. B. Cao, Y. W. Li, J. Wang, H. Jiao, *Surf. Sci.* **2007**, *601*, 1271–1284.

[20] L. Foppa, T. Margossian, S. M. Kim, C. Müller, C. Copéret, K. Larmier, A. Comas-Vives, *J. Am. Chem. Soc.* **2017**, *139*, 17128–17139.

[21] G. Sierra Gallego, C. Batiot-Dupeyrat, J. Barrault, F. Mondragón, *Ind. Eng. Chem. Res.* **2008**, *47*, 9272–9278.

[22] J. H. Kim, J. K. Kim, J. Liu, A. Curcio, J. Jang, I. Kim, F. Ciucci, W. Jung, *ACS Nano* **2021**, *15*, 81–110.

[23] D. Neagu, V. Kyriakou, I. L. Roiban, M. Aouine, C. Tang, A. Caravaca, K. Kousi, I. Schreur-Piet, I. S. Metcalfe, P. Vernoux, M. C. M. Van De Sanden, M. N. Tsampas, *ACS Nano* **2019**, *13*, 12996–13005.

[24] T. W. van Deelen, C. Hernández Mejía, K. P. de Jong, *Nat. Catal.* **2019**, *2*, 955–970.

[25] N. Bonmassar, M. F. Bekheet, L. Schlicker, A. Gili, A. Gurlo, A. Doran, Y. Gao, M. Heggen, J. Bernardi, B. Klötzer, S. Penner, *ACS Catal.* **2020**, *10*, 1102–1112.

Angew. Chem. Int. Ed. **2022**, *61*, e202204990 (9 of 10)

© 2022 The Authors. Angewandte Chemie International Edition published by Wiley-VCH GmbH

[26] V. R. Choudhary, B. S. Uphade, A. A. Belhekar, *J. Catal.* **1996**, *163*, 312–318.

[27] M. R. Goldwasser, M. E. Rivas, E. Pietri, M. J. Pérez-Zurita, M. L. Cubeiro, L. Gingembre, L. Leclercq, G. Leclercq, *Appl. Catal. A* **2003**, *255*, 45–57.

[28] U. Oemar, P. S. Ang, K. Hidajat, S. Kawi, *Int. J. Hydrogen Energy* **2013**, *38*, 5525–5534.

[29] Y. J. Su, K. L. Pan, M. B. Chang, *Int. J. Hydrogen Energy* **2014**, *39*, 4917–4925.

[30] M. M. Nair, S. Kaliaguine, F. Kleitz, *ACS Catal.* **2014**, *4*, 3837–3846.

[31] T. Nakamura, G. Petzow, L. J. Gauckler, *Mater. Res. Bull.* **1979**, *14*, 649–659.

[32] D. Neagu, G. Tsekouras, D. N. Miller, H. Menard, J. T. S. Irvine, *Nat. Chem.* **2013**, *5*, 916–923.

[33] R. D. Shannon, *Acta Crystallogr. Sect. A* **1976**, *32*, 751–767.

[34] S. Ramesh, N. J. Venkatesha, *ACS Sustainable Chem. Eng.* **2017**, *5*, 1339–1346.

[35] Y. Adachi, N. Hatada, K. Hirota, M. Kato, T. Uda, *J. Am. Ceram. Soc.* **2019**, *102*, 7077–7088.

[36] K. Ji, H. Dai, J. Deng, L. Song, S. Xie, W. Han, *J. Solid State Chem.* **2013**, *199*, 164–170.

[37] A. M. Tarditi, N. Barroso, A. E. Galetti, L. A. Arrúa, L. Cornaglia, M. C. Abello, *Surf. Interface Anal.* **2014**, *46*, 521–529.

[38] Y. X. Liu, S. F. Wang, Y. F. Hsu, H. W. Kai, P. Jasinski, *J. Eur. Ceram. Soc.* **2018**, *38*, 1654–1662.

[39] L. Xu, W. Liu, X. Zhang, L. Tao, L. Xia, X. Xu, J. Song, W. Zhou, X. Fang, X. Wang, *ChemCatChem* **2019**, *11*, 2887–2899.

[40] N. F. Khairudin, M. Mohammadi, A. R. Mohamed, *Environ. Sci. Pollut. Res. Int.* **2021**, *28*, 29157–29176.

[41] H. Gao, Z. Yao, Y. Shi, S. Wang, *Catal. Sci. Technol.* **2018**, *8*, 697–701.

[42] S. Khajeh Talkhoncheh, M. Haghighi, *J. Nat. Gas Sci. Eng.* **2015**, *23*, 16–25.

[43] C. Price, E. Earles, L. Pastor-Pérez, J. Liu, T. Reina, *Chemistry* **2019**, *1*, 3–16.

[44] Y. Sun, G. Zhang, J. Liu, Y. Xu, Y. Lv, *Int. J. Hydrogen Energy* **2020**, *45*, 640–649.

[45] Y. Shin, K. Y. Doh, S. H. Kim, J. H. Lee, H. Bae, S. J. Song, D. Lee, *J. Mater. Chem. A* **2020**, *8*, 4784–4789.